www.MaterialsViews.com

High-Quality, Ultraconformal Aluminum-Doped Zinc Oxide Nanoplasmonic and Hyperbolic Metamaterials

Conor T. Riley, Joseph S. T. Smalley, Kirk W. Post, Dimitri N. Basov, Yeshaiahu Fainman, Deli Wang, Zhaowei Liu, and Donald J. Sirbuly**

Aluminum-doped zinc oxide (AZO) is a tunable low-loss plasmonic material capable of supporting dopant concentrations high enough to operate at telecommunication wavelengths. Due to its ultrahigh conformality and compatibility with semiconductor processing, atomic layer deposition (ALD) is a powerful tool for many plasmonic applications. However, despite many attempts, high-quality AZO with a plasma frequency below 1550 nm has not yet been realized by ALD. Here a simple procedure is devised to tune the optical constants of AZO and enable plasmonic activity at 1550 nm with low loss. The highly conformal nature of ALD is also exploited to coat silicon nanopillars to create localized surface plasmon resonances that are tunable by adjusting the aluminum concentration, thermal conditions, and the use of a ZnO buffer layer. The high-quality AZO is then used to make a layered AZO/ZnO structure that displays negative refraction in the telecommunication wavelength region due to hyperbolic dispersion. Finally, a novel synthetic scheme is demonstrated to create AZO embedded nanowires in ZnO, which also exhibits hyperbolic dispersion.

C. T. Riley, Prof. D. J. Sirbuly
Department of NanoEngineering
University of California
San Diego, La Jolla, CA 92093, USA
E-mail: dsirbuly@ucsd.edu

J. S. T. Smalley, Prof. Y. Fainman,
Dr. D. Wang, Prof. Z. Liu
Department of Electrical and Computer Engineering
University of California
San Diego, La Jolla, CA 92093, USA
E-mail: z4liu@eng.ucsd.edu

K. W. Post, Prof. D. N. Basov
Department of Physics
University of California
San Diego, La Jolla, CA 92093, USA

Prof. Y. Fainman, Dr. D. Wang, Prof. Z. Liu, Prof. D. J. Sirbuly
Materials Science and Engineering
University of California
San Diego, La Jolla, CA 92093, USA

DOI: 10.1002/smll.201501797

1. Introduction

Plasmonic materials exhibit unique optical properties that originate from a strong coupling between the unbound electrons in the material and incident light.[1] Exploiting this light–matter interaction allows for the confinement of light below the diffraction limit and a large electric field enhancement leading to many exciting applications including surface-enhanced Raman spectroscopy,[2] hyperbolic dispersion,[3] cancer diagnostics and treatment,[4] and guidance of light in subwavelength features.[5] The majority of past plasmonic research has focused on noble metals such as gold and silver in the visible regime. However, because the plasma frequencies of noble metals are fixed, the plasmonic response of these materials in the near-infrared is limited. Therefore, alternative materials such as highly doped semiconductors have been gaining attention due to their tunable plasmonic properties that can be optimized for desired applications. Of all the

highly doped semiconductors under consideration, which includes silicon, germanium, III–V compounds (e.g., GaAs, InP, GaN), and metal oxides (e.g., ZnO, InO_2), aluminum-doped zinc oxide (AZO) has become a leading candidate for plasmonic applications since it has been shown to achieve doping levels high enough to exhibit plasmonic behavior at telecommunication wavelengths (≈1550 nm) with lower loss than any other material reported.[6] To date, the only AZO synthetic techniques which have generated plasmonic materials at 1550 nm are solution grown nanoparticles[7] and thin films created by pulsed laser deposition (PLD).[8] There are significant advantages with the AZO nanoparticles, given their simple synthetic protocols and scalability, however, creating complex geometries needed for many applications such as waveguiding and hyperbolic dispersion remains a major challenge. Fabricating advanced shapes and conformal coatings on nanostructures is also a limitation of PLD and it suffers from low scalability. Therefore, new fabrication techniques are required to enable the deposition of high-quality plasmonic coatings on nanoscale features.

One of the most versatile deposition techniques for conformally coating nanoscale features is atomic layer deposition (ALD) that utilizes a series of sequential, self-limiting surface chemical reactions by introducing chemical pulses into the reactor to form atomic monolayers.[9] Due to the nature of this process, ALD can create pin-hole free, scalable thin films that have an unmatched ability to fully conform to nanostructured surfaces. Furthermore, the dopant concentration can be easily controlled by adjusting the frequency at which the aluminum chemical pulse is applied. Unfortunately, despite many attempts,[10–12] ALD synthesized AZO films have yet to show plasmonic behavior at telecommunication wavelengths. Herein, for the first time, we show how thermally treated AZO protected by a thin HfO_2 layer can increase the carrier concentration to levels high enough to show plasmonic behavior at telecommunication wavelengths with corresponding optical losses that rival PLD AZO films. We also show how localized surface plasmonic resonances (LSPRs) can be tuned by varying the thermal conditions and adding ZnO buffer layers. Finally, we demonstrate the use of the high-quality AZO to synthesize two geometries required for hyperbolic metamaterials (HMMs).

The behavior of a plasmonic material is well described by the Drude model where the electrons are treated as a free electron gas or plasma.[13,14] Here the dielectric constant of a plasma is given as $\varepsilon(\omega)=1-\frac{\omega_p^2}{\omega^2}$ where ω_p is the bulk plasma frequency defined as

$$\omega_p=\sqrt{\frac{ne^2}{\varepsilon_0 m_e}} \tag{1}$$

In Equation (1), n is the majority carrier concentration, e is the charge of the electron, ε_0 is the free space permittivity, and m_e is the effective mass of the electron. By using a damping coefficient, γ and a background permittivity, ε_∞, to take into account electron collisions and the dielectric response of bound atomic charges, respectively, a complex expression for the dielectric constant of a plasmonic material can be written as

$$\varepsilon(\omega)=\varepsilon'+i\varepsilon''=\varepsilon_\infty-\frac{\omega_p^2}{\left(\omega^2+\gamma^2\right)}+i\frac{\omega_p^2\gamma}{\left(\omega^2+\gamma^2\right)\omega} \tag{2}$$

where the real part describes the polarization response of the material and the imaginary part describes the optical loss. The crossover wavelength is defined as the wavelength in which the real part is equal to zero. At incident energies lower than the crossover wavelength the polarization response of the plasma oscillations is fast enough to interact with the oscillation of incident electromagnetic radiation and the material behaves like a metal. At energies higher than the crossover wavelength the material becomes transparent and behaves as an insulator. Since both the dielectric response and the optical loss are proportional to n, an interesting opportunity exists to tune the plasmonic properties in semiconductors by adjusting the dopant concentration. In addition, for semiconductors, the carrier mobility, μ, can be related to the damping coefficient by $\gamma=\frac{e}{\mu m_e}$. Since the mobility is known to decrease with increasing impurity concentration due to electron-impurity scattering, an increase in the optical loss is expected by increasing the aluminum concentration in highly doped AZO. However, it should be noted that other factors are responsible for optical loss in addition to Drude dampening such as intra- and interband transitions, surface roughness, substrate adhesion, and metal-substrate contact surface area.[6,15]

At the interface between a metal and an insulator, collective oscillations of the free electrons can propagate creating a surface plasmon polariton (SPP). When the geometry of the material is much smaller than the incident wavelength, the SPP becomes localized creating an LSPR mode.[1] The LSPR mode is advantageous for many applications since it creates a large local heating and a large electric field enhancement at the metal/insulator surface. The LSPR properties can be explained by Mie theory that also shows that the resonant wavelength (wavelengths at which the extinction cross-section reaches a maximum) can be tuned by increasing the carrier concentration. Analogous to guided modes in dielectric resonators, the quality factor ($\frac{\lambda_r}{\Delta\lambda}$, where λ_r is the resonant wavelength and $\Delta\lambda$ is the full width half max of the resonance) of a plasmonic resonator can be tuned by varying the optical loss.[16,17]

Metamaterials are artificially designed materials engineered to have properties that do not exist in nature. Specifically, optical metamaterials have enabled the advancement of many applications such as optical magnetism, cloaking, and super resolution through the engineered combination of plasmonic and dielectric materials with features much smaller than the wavelength of light. Initial research utilized advanced 3D geometries to tailor both the magnetic permeability and electric permittivity to have negative values (double negative media) resulting in a negative index of refraction. However, fabricating 3D metamaterials that fulfil this size criterion in the NIR–Vis wavelength range presents a challenge. Therefore, many researchers have focused on

the use of HMMs in order to ease synthetic requirements. Unlike double negative media, HMMs utilize extreme optical anisotropy that arises from the combination of nonmagnetic materials with permittivity of opposing sign. In the limit of effective medium theory (EMT), the response of HMMs to transverse magnetic (TM) polarized light is described by a diagonal permittivity tensor, with two similar axes ($\varepsilon_{\parallel}$) and one unique axis ($\varepsilon_{\perp}$). Two possible types of HMMs thus emerge: Type I (transverse positive) where $\varepsilon_{\parallel} > 0, \varepsilon_{\perp} < 0$ and Type II (transverse negative) where $\varepsilon_{\perp} > 0,\ \varepsilon_{\parallel} < 0$. Although both types of HMMs support the propagation of high k-vector modes, each type has unique characteristics which can be advantageous to specific applications. For example, negative refraction and hyperlensing are only observed in type I HMMs[18,19] while higher reflectivity is observed in type II HMMs.[20] The latter feature makes type II useful for asymmetric transmission[21] as well as gain-compensated waveguiding.[22] Such materials are typically created by two prominent geometries, as shown in **Figure 1**: a planar layered structure in which alternating layers of plasmonic and dielectric materials are stacked or a wire structure in which plasmonic nanowires are embedded in a dielectric media. In both cases, the characteristic dimensions (layers thickness or wire diameter) must be much smaller than the wavelength of incident light. The layered geometry has the advantage of simpler fabrication. On the other hand, the nanowire geometry has the advantage of displaying type I properties away from resonance providing lower loss which may greatly benefit hyperlensing applications.[23] Furthermore, the nanowire geometry has been demonstrated to be a superior biosensor compared to conventional SPP-based devices.[24]

In the limit of EMT, the properties of HMMs depend only on the metal filling fraction as well as the permittivity of the dielectric and metallic materials. For the layered structure, the transverse and longitudinal permittivity elements are

$$\varepsilon_{\parallel} = f\varepsilon_{\mathrm{m}} + (1-f)\varepsilon_{\mathrm{d}};\quad \varepsilon_{\perp} = \left(\frac{f}{\varepsilon_{\mathrm{m}}} + \frac{1-f}{\varepsilon_{\mathrm{d}}}\right)^{-1} \tag{3}$$

where f is the filling fraction of the metallic component, and ε_{m} and ε_{d} are the permittivity of the metallic and dielectric materials, respectively. For the nanowire structure, the permittivity elements arising from the Maxwell–Garnet approximation are

$$\varepsilon_{\parallel} = \frac{\left[(1+f)\varepsilon_{\mathrm{m}} + (1-f)\varepsilon_{\mathrm{d}}\right]\varepsilon_{\mathrm{d}}}{(1-f)\varepsilon_{\mathrm{m}} + (1+f)\varepsilon_{\mathrm{d}}};\quad \varepsilon_{\perp} = f\varepsilon_{\mathrm{m}} + (1-f)\varepsilon_{\mathrm{d}} \tag{4}$$

The majority of HMMs utilize either noble metals operating in the visible spectrum or semiconductors in the mid-infrared. PLD synthesized AZO/ZnO multilayer HMMs have recently been reported with high-quality factors operating in the NIR owing to their low loss.[18] Here we show that thermally processed ALD AZO films are fully capable of creating both the layered and nanowire geometries required for hyperbolic dispersion which is difficult to do with other fabrication techniques. Because of the superb coating capabilities of ALD, and our proven ability to deposit high-quality plasmonic materials in the NIR, our synthetic method has distinct advantages for fabricating HMMs. First, the film thickness in the layered structures can be controlled at the subnanometer level. Second, the films grown via ALD are smooth and pinhole free. Lastly, ALD deposits the most conformal coatings compared to other thin deposition techniques, which allows for the study of advanced geometries such as complex nanostructures or cylindrical waveguide claddings.[25]

2. Results and Discussion

Previously we demonstrated the synthesis and plasmonic tunability of AZO films created by ALD.[12] However, attaining thin films (< 60 nm) with crossover wavelengths below 2100 nm and low loss ($\varepsilon'' < 1$) could not be achieved. The shortest crossover wavelength obtained for a 56 nm film was at 2160 nm with a corresponding ε'' of ≈2. To improve these properties we have investigated the effects of thermal pulses by rapid thermal processing (RTP). It was found that any thermal processing over 500 °C on the as-made AZO led to a decrease in the carrier concentration. However, if a 10 nm or thicker film of HfO_2 was deposited over the AZO by ALD, the crossover wavelength could be tuned to higher energies and lower losses after RTP up to 900 °C. **Figure 2** compares the optical constants obtained from ellipsometry for two 56 nm HfO_2-coated AZO films, one with (AZO-TP) and the other without (AZO) a post-synthetic thermal treatment at 825 °C for 15 s. After the RTP treatment the crossover wavelength shifts by

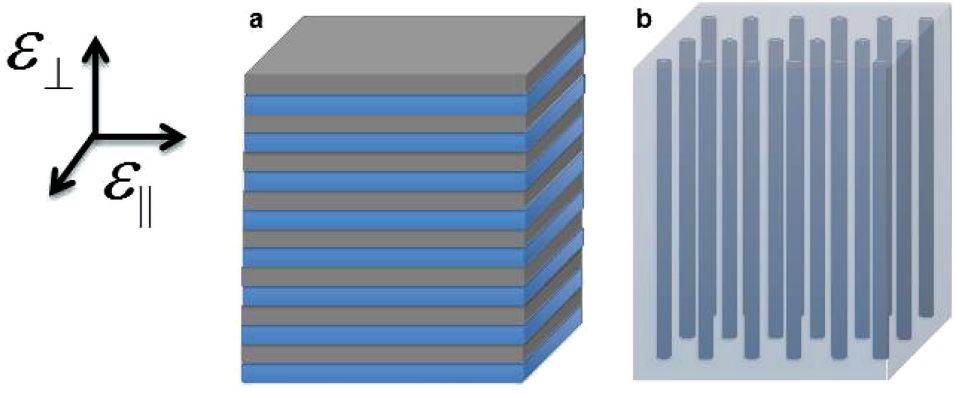

Figure 1. Schematics of a) multilayer and b) nanowire array geometries capable of hyperbolic dispersion.

small NANO MICRO

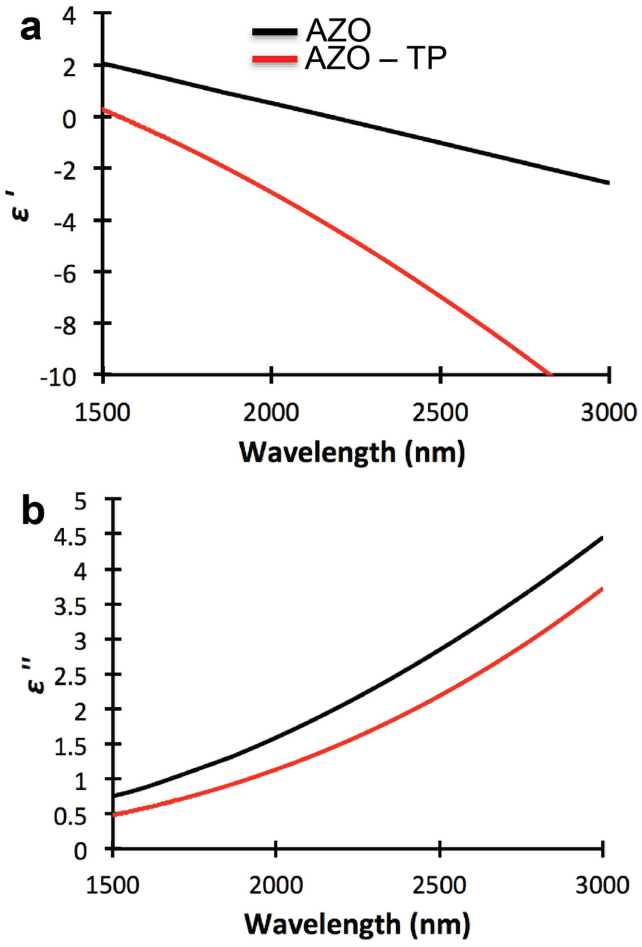

Figure 2. a) Real and b) imaginary dielectric constants of AZO and thermally processed AZO at 825 °C for 15 s. Both samples are coated with HfO_2.

over 600 nm from 2150 to 1545 nm. In addition, the losses for the thermally treated films are significantly reduced. According to the Drude theory, a blueshift in the crossover wavelength should be accompanied by an increase in the carrier concentration (Equation (2)). Therefore, Hall measurements were carried out on thermally processed and as-made AZO/HfO_2 films (600/12 nm). In order to ensure that the bulk AZO material was probed, the HfO_2 layer was removed by reactive ion etching (RIE). Subsequently, the top 100 nm of the AZO was removed by wet etching to ensure that no contaminants from the RIE process were present. The results of the Hall measurements are summarized in **Table 1** which show that the carrier concentration increases from 1.0×10^{21} to 1.5×10^{21} cm^{-3} after thermal processing. Consequently, ultralow resistivity films are created after thermal processing with a resistivity of 3.8×10^{-4} Ω·cm, which to the best of our knowledge is the lowest reported value for ALD-synthesized AZO. The Drude model fitting parameters of nonthermally processed and thermally processed AZO (825 °C, 15s) are also listed in Table 1 which shows an increase in ω_p and a decrease in γ after thermal processing, qualitatively consistent with the optical constants described in Figure 2 and the carrier concentration values obtained from Hall measurements.

Further investigation into the enhanced carrier concentrations was carried out through photoluminescence (PL) studies. Information about the defect concentration of ZnO-based materials can be inferred by examining the visible portion of the PL emission spectrum. The most commonly referred defects in ZnO are oxygen vacancies (V_o), zinc interstitials (Zn_i), oxygen interstitials (O_i), oxygen antisites (O_{Zn}), and zinc vacancies (V_{Zn}).[26,27] V_o and Zn_i are known to be electron donating whereas O_i, V_{Zn}, and O_{Zn} are found to be electron accepting. Here, to ensure that the PL signal was coming only from the AZO, RIE was carried out to remove the HfO_2 protection layer.

As seen in **Figure 3**, films thermally processed at 825 °C for 15 s without the HfO_2 layer show a strongly enhanced PL signal at 600 nm. This PL emission is attributed to the O_i defects, which has been observed previously for thermally treated ZnO at 700 °C.[28] The formation of these particular defects has been reported to be caused by the creation of metallic zinc and its subsequent evaporation leaving behind accepting O_i defects that reduce the carrier concentration.[29] On the other hand, the AZO films thermally processed with the HfO_2 layer show a slight decrease in the visible defect emission. This supports the argument that the HfO_2 serves as a protection layer preventing zinc evaporation. However, this does not explain why the carrier concentration increases after thermal processing. In addition to the Hall measurements for AZO, Table 1 also reports the results for pure ZnO. In contrast to AZO films, the ZnO carrier concentration decreases after thermally treating the HfO_2-protected samples. This suggests that carrier enhancement in the AZO is due to the activation of the aluminum dopants. It has been demonstrated that the amount of aluminum atoms contributing free electrons is far lower for ALD than other synthetic methods.[30,31] Using an effective field model, it has been proposed that this discrepancy is due to the unique layer-by-layer configuration of aluminum dopants[31] as opposed to randomly oriented dopants in other methods such as chemical vapor deposition,[32] PLD,[33] or sputtering.[34] This model shows that the close proximity of adjacent aluminum

Table 1. Hall measurement results for AZO and ZnO, along with Drude model fitting parameters for AZO, before and after rapid thermal processing. All samples were thermally processed with a 12 nm HfO_2 protection layer. The protection layer was removed before carrying out the Hall measurement.

	$n \times 10^{21}$ [cm^{-3}]	μ [$cm^2 V^{-1} \cdot s^{-1}$]	$\rho \times 10^{-4}$ [Ω·cm]	ε_∞	ω_p [eV]	γ [eV]
AZO Before RTP	1.0	10.1	6.1	4.05	1.28	0.28
AZO After RTP	1.5	9.8	3.8	4.5	1.70	0.096
ZnO Before RTP	0.029	16.5	127.2	–	–	–
ZnO After RTP	0.0087	16.8	429.7	–	–	–

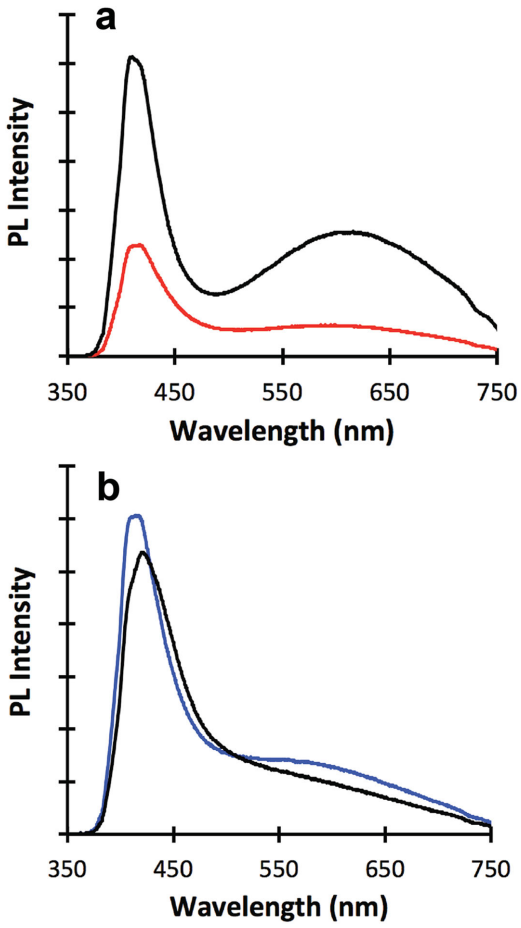

Figure 3. a) PL spectrum of an unprotected AZO film before (red) and after (black) thermally processing at 825 °C for 15 s. b) PL spectrum of an AZO film protected with HfO_2 before (blue) and after (black) thermally processing at 825 °C for 15 s.

atoms causes electronic repulsion that suppresses the donation of free electrons and decreases the carrier concentration.[31] Therefore, we hypothesize that the boost in carrier concentration after the thermal processing is caused by the diffusion of aluminum atoms into the ZnO layers configuring the dopants into randomly oriented positions more suitable for supporting higher carrier concentrations. Experimentally derived diffusion constants from the literature[35] support this theory by showing that the aluminum atoms are capable of traveling more than one half of a ZnO/Al_2O_3 period (≈2 nm) under the thermal conditions used in our experiments.

In our previous report, we deposited the unprotected AZO onto silicon nanoparticles (SiNPs) created by nanosphere lithography (NSL) to investigate the LSPR modes.[12] Here, we use the same approach to verify our results and show how adjusting the thermal conditions can tune and increase the quality factor of the LSPR for protected AZO films. We demonstrate this using an SiNP array template with an average length, diameter, and pitch of 702, 201, and 445 nm, respectively. The standard deviation of the SiNP diameter was found to be 34 nm. Although this size distribution is significant, it has been found to have no impact on the LSPR modes.[12] After fabricating the nanopillars they were coated with a 56 nm thick layer of AZO and 12 nm of HfO_2 (**Figure 4**). **Figure 5**a shows the LSPR of both as-made (25 °C) and thermally processed AZO coated/protected SiNPs. Consistent with the ellipsometric data discussed earlier, a clear blueshift is observed after thermal processing indicating an increase in carrier concentration. In addition, due to smaller losses in the postprocessed AZO, the quality factor is increased. Moreover, the tuning of the LSPR is demonstrated in Figure 5a–c. First, by varying the thermal processing temperature (15 s) it is clear that there is a significant blueshift and increase in the quality factor in the temperature range of 700–900 °C (Figure 5a). Below 700 °C, little change is observed and above 950 °C the LSPR is no longer observed within the wavelength range probed. We find that the largest blueshift occurs between 825 and 900 °C. Moreover, when the temperature is held constant at 825 °C and the time is varied the ideal conditions are found to be 15–30 s (Figure 5b). Less than 15 s the aluminum atoms are not fully activated and the carrier concentration is still increasing. Above 30 s the quality factor of the peak begins to decrease. Therefore, we find that the optimal thermal conditions for lowest loss and highest energy crossover wavelength are achieved when the protected AZO films are processed at 825 °C for 15 s. We believe that at these thermal conditions aluminum is allowed to migrate into a configuration that supports higher carrier concentration while suppressing donating defects. Moreover, ε'' is reduced by improved

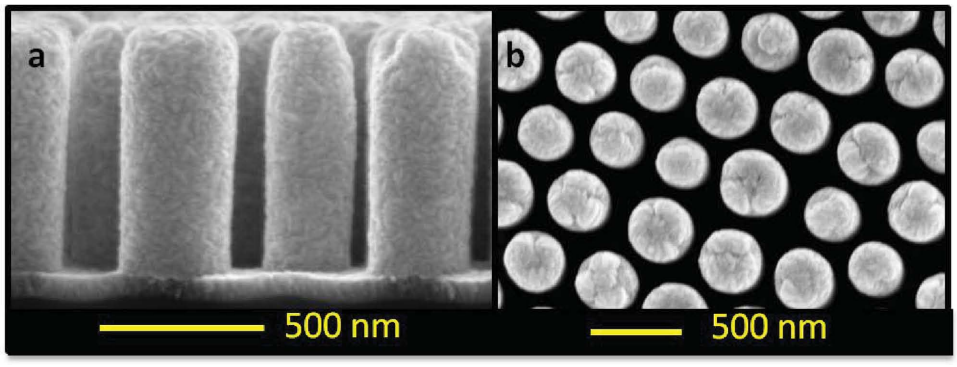

Figure 4. a) Cross-sectional and b) top-down SEM image of an SiNP array coated by an AZO/HfO_2 (56/12 nm) film.

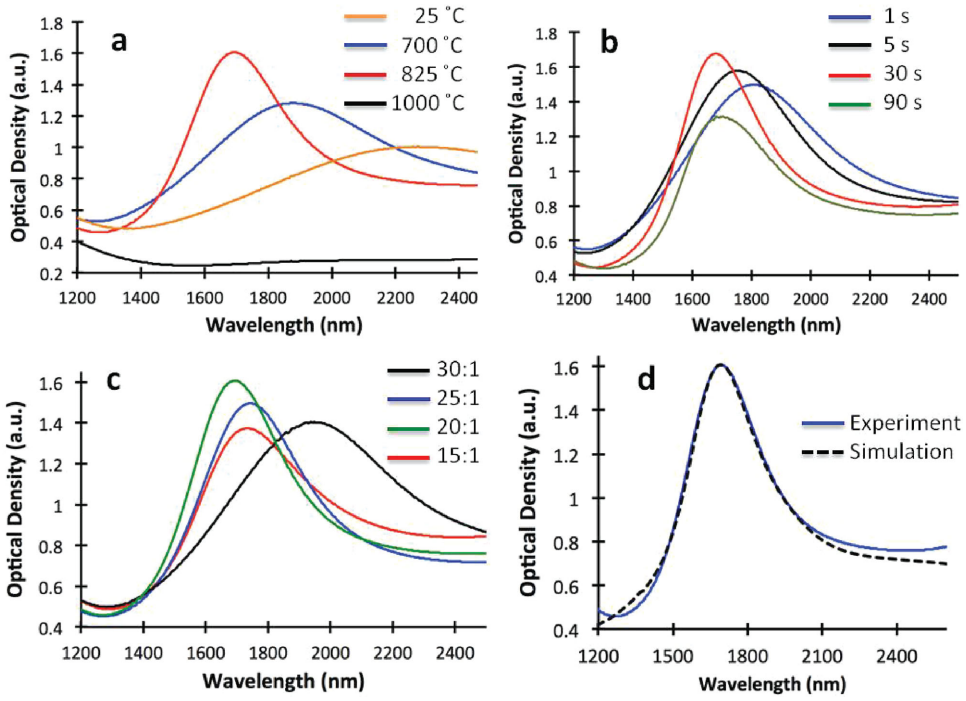

Figure 5. IR extinction spectra of thermally processed AZO/HfO_2 (56/12 nm) after deposition on an SiNP array and a) treated with a 15 s thermal pulse with varying temperatures, b) held at a constant temperature of 825 °C but varying pulse times, and c) treated with a varying Al:Zn compositions (825 °C, 15 s). d) Comparison of experimental IR extinction spectra and an FDTD simulation of an AZO/HfO_2 (56/12 nm) layer coated on an SiNP (in experiment the sample was thermally processed at 825 °C for 15 s).

AZO-substrate adhesion and/or improvements in the crystal structure. However, the exact mechanism for the improvements is still under investigation. In addition, similar to the nonprocessed AZO, the LSPR properties can also be tuned by adjusting the aluminum dopant concentration. Here the maximum blueshift and quality factor are achieved at a 20:1 Zn:Al chemical pulse ratio (Figure 5c). At higher aluminum concentrations, the carrier concentration is found to decrease most likely due to aluminum suboxide formation and clustering.[34] Importantly, controls were carried out on thermally treated samples that included SiNPs coated with only HfO_2 and SiNPs coated with ZnO/HfO_2 which did not show any optical activity in the NIR region (Figure S1, Supporting Information).

In order to further investigate the LSPRs in the AZO/HfO_2 coated SiNP samples, finite-difference time-domain (FDTD) simulations were carried out using the optical constants obtained from ellipsometry and on dimensions identical to those measured in the experiments. As shown in Figure 5d there is excellent agreement between the simulation and experimental data for both the spectral positioning and quality factor. Since experimentally removing the HfO_2 from the sidewalls is extremely difficult, and enhanced plasmonic properties with protection layers below 10 nm are not observed, the impact of the HfO_2 on the LSPR was studied through the FDTD simulations. The data show that a 12 nm HfO_2 layer shifts the resonant wavelength by 25 nm due to a larger dielectric constant of the media surrounding the AZO (Figure S2, Supporting Information). However, the linewidth stays relatively the same indicating the HfO_2 does not increase the quality factor due to any cladding effects.

The effects on the conductivity of aluminum-doped[36] and gallium-doped[37] ZnO films due to ZnO buffer layers (intermediate layer between substrate and AZO) have previously been studied. It has been shown that the grain size of ZnO buffer layers becomes larger with increasing thickness, which translates to AZO film growth with larger grain sizes. Larger grain sizes decrease the amount of grain boundaries that create electronic traps and barriers, which results in a more conductive film. This generates highly conductive AZO films that arise from an increase in both the carrier concentration and electron mobility. Therefore, according to Drude theory, a blueshift in the crossover wavelength and lower loss is expected by the use of ZnO buffer layers. **Figure 6**a,b demonstrates this effect for HfO_2-protected and thermally processed (825 °C, 15 s) 56 nm AZO films. Here the crossover wavelength shifts from 1545 to 1450 nm when a 112 nm ZnO buffer layer is used. In addition, the optical loss is significantly decreased from 0.53 to 0.46 at 1550 nm. These properties are further verified by observing the effects of the LSPR modes on the SiNPs for protected 20 nm AZO films thermally processed at 825 °C for 15 s. Here the resonant wavelength is shifted from 1670 nm to telecommunication wavelengths (≈1550 nm) by adding a 50 nm ZnO buffer layer (Figure 6c).

To demonstrate hyperbolic dispersion with the ALD grown films, we first investigated a simple layered structure comprised of eight periods of ZnO and AZO alternating stacks grown on silicon (**Figure 7**). The thickness of each layer is 56 nm giving a total thickness of 896 nm. After growing

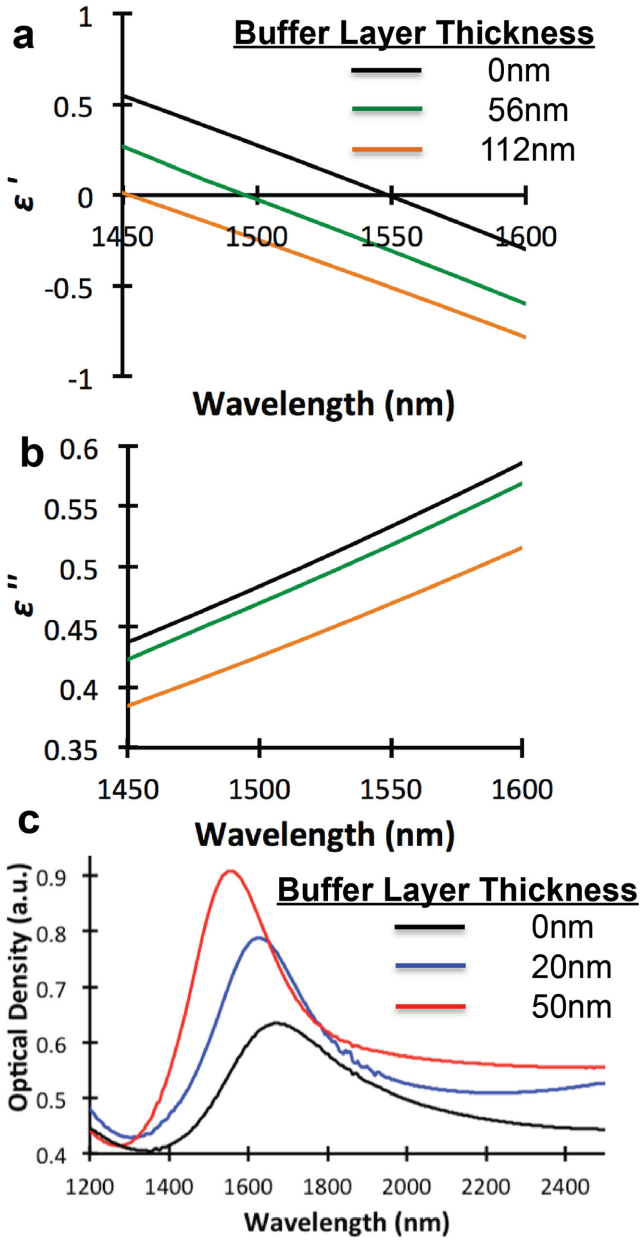

Figure 6. a) Real and b) imaginary dielectric constants for thermally processed AZO films with varying ZnO buffer layer thicknesses. c) IR extinction spectra of thermally processed AZO/HfO_2 (20/12 nm) layer deposited on an SiNP array with varying ZnO buffer layer thicknesses.

the HMM, it was protected with a 50 nm layer of HfO_2 and annealed at 825°C for 20 s. The electron image in Figure 7a captures the contrast between the alternating AZO and ZnO layers. Using the permittivities obtained for AZO grown on a 112 nm ZnO buffer layer, EMT (Equation (3)) predicts type I hyperbolic dispersion from 1460 to 2000 nm and type II dispersion for wavelengths longer than 2080 nm (Figure S3, Supporting Information). In order to show the functionality of the high-quality HMM films, we demonstrated negative refraction using the well-known razor blade experiment.[18,38] In this experiment the sample was placed between a light source and a detector and the transmission was studied at different angles in the presence and absence of a razor blade that blocks half of the light transmitted through the sample (Figure 7b). Therefore, with this configuration, if negative refraction occurs the light is shifted away from the razor blade so that more light is incident upon the detector causing a peak in the transmission ratio of the partially blocked beam/full beam for TM-polarized light only. As expected, a clear peak is observed for TM-polarized light (Figure 7c) while transverse-electric (TE) polarized light shows no peaks (Figure S4, Supporting Information). The transmission data also show good agreement with FDTD simulations that were carried out on the identical layered structure using the permittivities of AZO grown on 112 nm ZnO buffer layers. As predicted by EMT, none of the properties depend on the thickness of each individual layer as samples with layer thicknesses as thin as 15 nm were synthesized with little impact on the negative refraction performance. In addition, analytical calculations based on both the transfer matrix (TMM) and scattering matrix (SMM) methods confirm the experimental and FDTD results. The angle of refraction determined using the derivative of the transmitted phase with respect to the angle of incidence[39] is shown in Figure 7d. The complex amplitude transmittance is calculated via the TMM[40] using the experimentally obtained optical constants. Additionally, the refraction angle predicted by EMT is shown. The predicted angle of maximum negative refraction, and therefore the largest transmission ratio, is slightly redshifted from the experimental results. The small discrepancy is likely due to the approximation of the method where accuracy depends upon the total thickness of the multilayer.[41]

The SMM, while generally more difficult to implement than the TMM, is known to be more accurate.[42] Figure S5 (Supporting Information) compares the squared magnitude of both TE- and TM-polarized electric fields, incident at an angle of 25°, for several different wavelengths. The fields are determined using a modified version of an open-access SMM implementation.[43] The incident beam undergoes greatest negative refraction at a wavelength of 1470 nm, in very good agreement with experimentally observed transmission ratio. For clarity, only the real parts of the experimentally determined optical constants are used and the structure consists of 50 periods of alternating 56 nm thick ZnO and AZO layers. It is clear from an analysis of TE and TM fields at various angles of incidence with a fixed wavelength of 1470 nm that only the TM mode undergoes negative refraction (Figure S7, Supporting Information).

Lastly, we further exploited the conformal properties of ALD to fabricate the nanowire geometry required for HMM. To accomplish this we first employed NSL to create a silicon nanopillar array. The gaps were then filled with ZnO (**Figure 8**a) that was etched using RIE to expose the silicon on the top of the nanopillars. RIE was used again with a different gas composition to remove the silicon nanopillars leaving nanoholes (Figure 8b). The nanoholes were then filled with AZO and the top layer of AZO was removed to improve the transmission (Figure 8c). The average length, pitch, and diameter of the AZO nanowires were 907, 407, and 250 nm, respectively. As seen in Figure 8d, this leads to an AZO filling fraction of 0.3. EMT (Equation (4)) predicts type II hyperbolic dispersion from 1.84 to 2.32 μm and

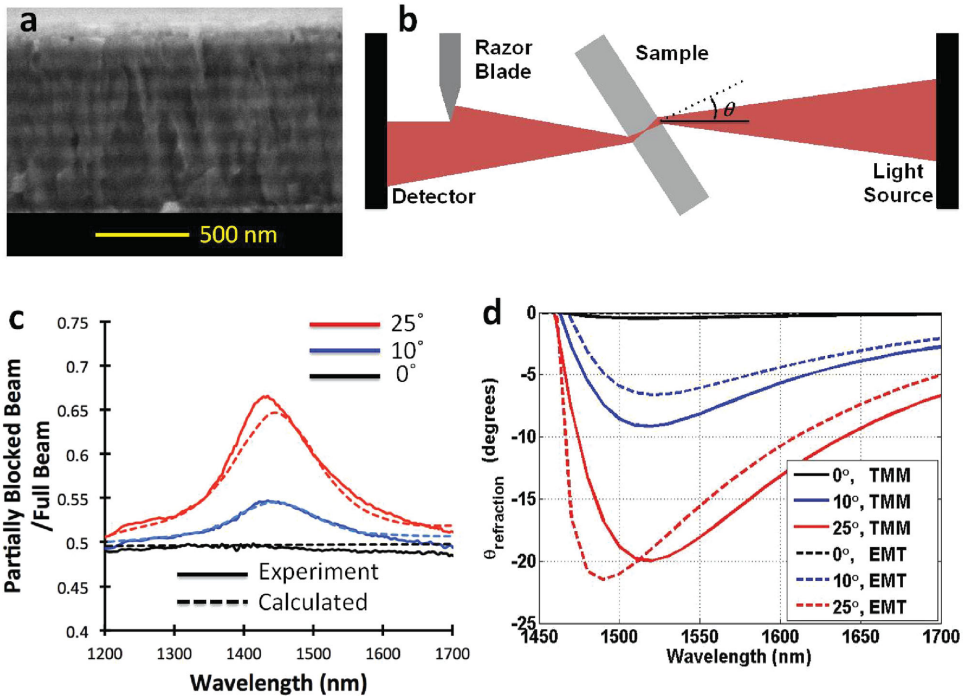

Figure 7. a) SEM image of multilayer ZnO/AZO HMM comprised of 8 ZnO/AZO (56/56 nm) layers in the case of negative refraction. b) Schematic of the negative refraction experiment. c) TM polarization transmission ratio of partially blocked beam/full beam showing a clear peak indicative of negative refraction. d) Angle of refraction predicted by EMT and TMM.

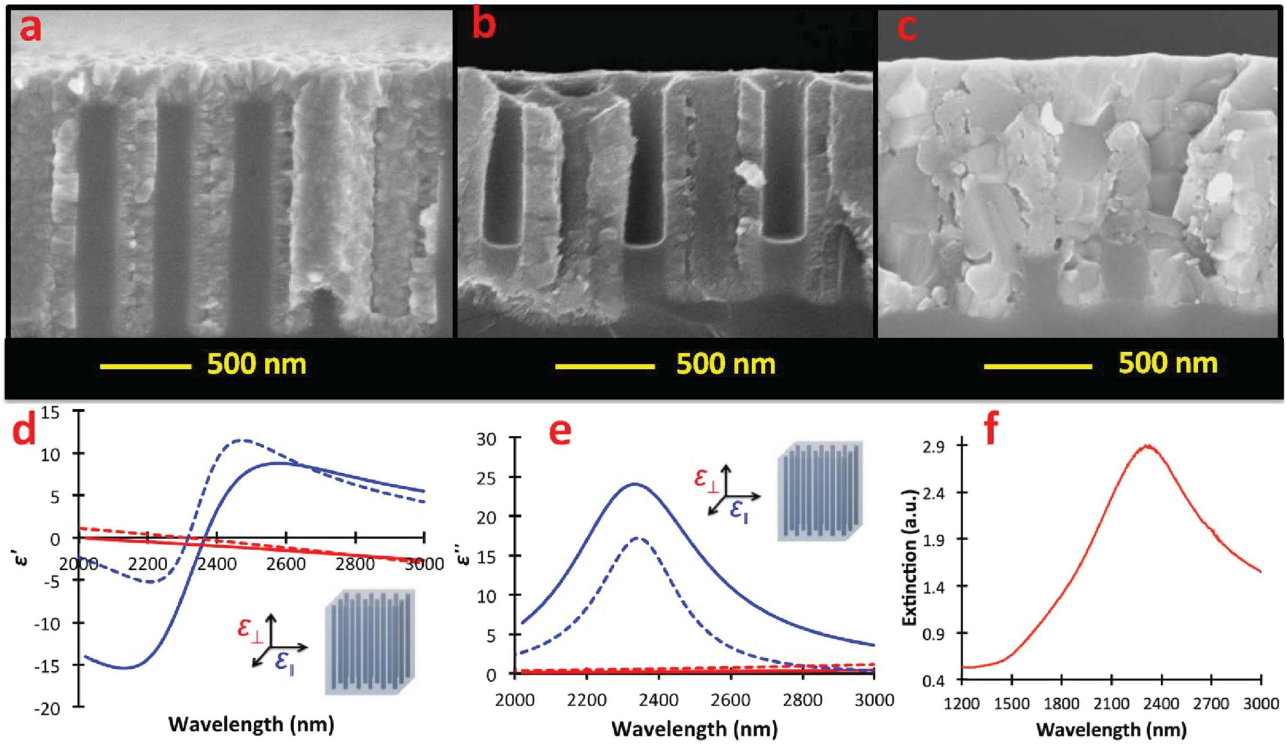

Figure 8. SEM images taken at different steps during the fabrication of AZO nanowires embedded in ZnO including a) ZnO-coated silicon nanowires, b) etched silicon leaving behind nanoholes, and c) AZO-filled nanoholes. d) Real and e) imaginary optical constants as predicted by EMT (dashed) and extracted from ellipsometry (solid). f) IR extinction spectra of AZO nanowires embedded in ZnO showing optical losses identical to that predicted by EMT.

type I hyperbolic dispersion at wavelengths longer than 2.58 μm. Extracted values from ellipsometry (Figure 8d,e) show similar behavior as predicted from EMT. However, discrepancies are expected due to rough nanowire walls and the polycrystalline structure of the AZO generated via ALD. The extinction measurements (Figure 8f) show a clear peak centered at 2335 nm which is in an identical location to where the maximum loss is predicted by EMT for this geometry.

3. Conclusions

In conclusion, we have described a synthetic strategy for significantly improving the plasmonic properties of ALD-deposited AZO. The technique utilizes a simple protection layer and thermal treatment to decrease the optical loss of the films and blueshift the crossover wavelength to NIR wavelengths. The enhancement in the optical properties of the material is explained by allowing the migration and subsequent activation of aluminum dopants within the ZnO matrix while preventing the formation of donating defects through the use of a HfO_2 protection layer. The combination of high-quality plasmonic films with the advantages of ALD processing was exploited to create highly conformal films on an SiNP template created by NSL. The LSPR modes were validated through FDTD simulations and were shown to be highly tunable by varying the dopant concentration, thermal processing time, deposition temperature, and ZnO buffer layer thickness. Additionally, we showed that these material processes are fully capable of creating both layered and embedded nanowire HMMs. We note that the novel synthetic scheme displayed for embedded nanowire HMMs is able to produce embedded nanowires with any combination of materials that are available for ALD. These results introduce new strategies for fabricating ultraconformal, high-quality plasmonic nanomaterials and HMMs for NIR-enhanced light emission that cannot be achieved by other fabrication techniques. In addition to the plasmonic properties, the thermally processed AZO materials were found to have the lowest reported electrical resistivity for ALD-deposited AZO which has immediate implications on energy-related systems such as photovoltaics, photocatalysts, light emitting diodes, and thin film electronics.

4. Experimental Section

AZO Fabrication: ALD was carried out at using a Beneq TFS200 ALD system operating at a reactor temperature of 250 °C. Diethylzinc, trimethylaluminum, and water were used as the zinc, aluminum and oxygen sources, respectively, to grow the AZO films. The HfO_2 films were grown with tetrakis(dimethylamido)hafnium(IV) and water as the hafnium and oxygen sources, respectively. Alternating chemical pulses of metal and oxygen sources were released into the reactor. The amount of aluminum doped into ZnO was determined by how often an aluminum pulse was replaced with a zinc pulse. Unless specified otherwise, all films were grown at a 20:1 Zn:Al chemical pulse ratio. All film thicknesses were obtained on planar silicon substrates via ellipsometry using a Rudolph Auto EL Ellipsometer. After growth, RTP was done using an AG Associates Heat Pulse 610 with a 1.5 L min^{-1} nitrogen flow rate. The maximum ramp up and ramp down speeds were used which took less than 15 s to reach the maximum temperature and less than 20 s to cool down to 300 °C.

Optical and Electrical Characterization of AZO Films: In order to obtain the optical constants of the ALD-deposited materials, all films were deposited on RCA cleaned p-type (5 Ω·cm) single-sided polished, prime silicon. The ellipsometric constants (ψ and Δ) were measured in the range from 1200 to 1600 nm using a commercially available Woollam ellipsometer. Measurements were extended to longer wavelengths (1600–3000 nm) using a second J.A. Woollam IR ellipsometer coupled to a Bruker v/66s Fourier transform infrared spectrometer. In order to obtain the optical constants for the multilayer samples (Si/AZO/HfO_2 and Si/ZnO/AZO/HfO_2), ellipsometry was first preformed on the bare, cleaned silicon. Next, the optical constants of ZnO and HfO_2 were obtained from Si/HfO_2 and Si/ZnO samples. The complex permittivity of AZO was then obtained by modeling the multilayer system where AZO was the only unknown. All models were carried out on the J.A. Woollam VASE software where Kramers Kronig consistent oscillators were fit to the experimentally obtained ψ and Δ values. Hall measurements were performed on a home-built setup using the van der Pauw method at room temperature with a magnetic field of 3000–5000 G. Silver ohmic contacts were used for all samples. Both 600 nm AZO and ZnO samples were deposited on sapphire and coated with 12 nm of HfO_2. HfO_2 layers were removed using RIE via an Oxford P80 with CHF_3 and Ar gases. The top ≈100 nm of ZnO-based material was removed using dilute hydrochloric acid. The remaining thickness (≈500 nm) was confirmed by ellipsometry. All PL measurements were taken from films deposited on RCA cleaned p-type (5 Ω·cm) prime silicon. To characterize the defect emission, the HfO_2 layers were first removed by RIE. Next, dilute HCl was used to etch away any contaminates from the RIE process. The samples were then excited with a continuous-wave helium cadmium laser (Kimmon electric) and the PL spectra were captured using a thermoelectrically cooled (–75 °C) Princeton Instrument spectrometer. The laser beam was focused onto the sample (≈50 μm spot size) at an angle of 45° and power density of ≈1 W cm^{-2}.

Nanostructure Fabrication and Characterization: SiNP arrays were fabricated using NSL by a method adapted from the literature.[44] Silica nanoparticles (≈440 nm diameter) were grown by the well-known Stöber process.[45] Next, the particles were functionalized with aminopropyl-methyldiethoxysilane and deposited onto p-type (5 Ω·cm) prime silicon using a Langmuir Blodgett trough. The silica particles were then shrunk using RIE with CHF_3 and Ar gases using an oxford P80. Next, using an Oxford P100 with SF_6 and C_4F_8 gases, the exposed silicon was etched creating nanopillars. Any remaining SiO_2 was removed using hydrofluoric acid. Before ALD, all samples were cleaned using the RCA cleaning procedure. All extinction measurements were carried out from 1200 to 2500 nm on the nanopillar array using a Perkin Elmers Lambda 1050. FDTD simulations were carried out using the Lumerical software package. A single AZO/HfO_2 core shell nanopillar was modeled with periodic boundary conditions using identical dimensions to those observed in the experiments. Plane wave excitation was launched at normal incidence. All nanostructure imaging was carried out using an FEI XL30 ultrahigh resolution SEM.

HMM Fabrication and Characterization: Layered HMMs were synthesized on DSP and SSP p-type (5 Ω·cm) prime silicon. Eight periods (16 total layers) of alternating ZnO and AZO films were grown at 250 °C and capped with a 50 nm HfO_2 protection layer. All AZO components were grown with a 20:1 Zn:Al ratio. The whole sample was then thermally processed at 825 °C for 20 s. Negative refraction tests were carried out using a Perkin Elmer Lambda 1050. The sample was placed at the halfway point between the monochromator exit and PbS detector and the angle of the sample was varied from 0° to 20°. The beam was partially blocked by placing a razor blade at the halfway point between the sample and the detector such that the TE polarization at 0° was half of the full beam transmission. Embedded AZO nanowires were created by first synthesizing a nanowire template using NSL as described above. Next, 200 nm of ZnO was deposited at 250 °C to fill in the gaps. The top layer of ZnO was removed by RIE with CHF_3 and Ar gases using an oxford P80 to expose the silicon nanowire tips. Next, using an Oxford P100 with SF_6 and C_4F_8 gases, the exposed silicon was etched leaving nanoholes. The holes were filled with AZO at a 20:1 Zn:Al ratio at 250 °C and capped with a 50 nm HfO_2 protection layer. The sample was then thermally processed at 825 °C for 20 s and the top layer of HfO_2 and AZO was removed using RIE. Extracted optical constants were obtained using ellipsometry as described above. All models were carried out on the J.A. Woollam VASE software using a uniaxial model where Kramers Kronig consistent oscillators were fit to the experimentally obtained ψ and Δ values.

Supporting Information

Supporting Information is available from the Wiley Online Library or from the author.

Acknowledgements

This project was funded by a grant from the Blasker Science & Technology program of The San Diego Foundation (Grant #BLSK201252049). The authors would like to acknowledge Dr. Bernd Fruhberger, Larry Grissom, and Dr. Xuekun Lu of Calit2 at UCSD for their support in installing and calibrating the necessary precursor lines in the ALD system.

[1] S. A. Maier, *Plasmonics: Fundamentals and applications*, Springer, New York **2007**.
[2] B. Sharma, R. R. Frontiera, A.-I. Henry, E. Ringe, R. P. Van Duyne, *Mater. Today* **2012**, *15*, 16.
[3] A. Poddubny, I. Iorsh, P. Belov, Y. Kivshar, *Nat. Photonics* **2013**, *7*, 948.
[4] S. Lal, S. E. Clare, N. Halas, *Acc. Chem. Res.* **2008**, *41*, 1842.
[5] D. K. Gramotnev, S. I. Bozhevolnyi, *Nat. Photonics* **2010**, *4*, 83.
[6] G. V. Naik, V. M. Shalaev, A. Boltasseva, *Adv. Mater.* **2013**, *25*, 3264.
[7] G. Garcia, R. Buonsanti, A. Llordes, E. L. Runnerstrom, A. Bergerud, D. J. Milliron, *Adv. Opt. Mater.* **2013**, *1*, 215.
[8] J. Kim, G. V. Naik, N. K. Emani, U. Guler, A. Boltasseva, *IEEE J. Sel. Top. Quantum Electron.* **2013**, *19*, 4601907.
[9] S. M. George, *Chem. Rev.* **2010**, *110*, 111.
[10] A. K. Pradhan, R. M. Mundle, K. Santiago, J. R. Skuza, B. Xiao, K. D. Song, M. Bahoura, R. Cheaito, P. E. Hopkins, *Sci. Rep.* **2014**, *4*, 6415.
[11] A. Frolich, M. Wegener, *Opt. Mater. Express* **2011**, *1*, 883.
[12] C. T. Riley, T. A. Kieu, J. S. T. Smalley, S. H. A. Pan, S. J. Kim, K. W. Post, A. Kargar, D. N. Basov, X. Pan, Y. Fainman, D. Wang, D. J. Sirbuly, *Phys. Status Solidi RRL* **2014**, *8*, 948.
[13] N. W. Ashcroft, N. D. Mermin, *Solid State Physics*, Saunders College, Philadelphia, PA, USA **1976**.
[14] P. Drude, *Ann. Phys.* **1900**, *1*, 566.
[15] M. Bosman, L. Zhang, H. Duan, S. F. Tan, C. A. Nijhuis, C. W. Qiu, J. K. W. Yang, *Sci. Rep.* **2014**, *4*, 5537.
[16] S. A. Maier, *Opt. Quantum Electron.* **2006**, *38*, 257.
[17] M. J. Ford, M. G. Blaber, M. D. Arnold, N. Harris, M. B. Cortie, *Phys. B* **2007**, *394*, 184.
[18] G. V. Naik, J. Liu, A. V. Kildishev, V. M. Shalaev, A. Boltasseva, *Proc. Natl. Acad. Sci. USA* **2012**, *109*, 8834.
[19] I. V. Lindell, S. A. Tretyakov, K. I. Nikoskinen, S. Ilvonen, *Microwave Opt. Technol. Lett.* **2001**, *31*, 129.
[20] C. L. Cortes, W. Newman, W. Molesky, Z. Jacob, *J. Opt.* **2014**, *16*, 129501.
[21] T. Xu, H. J. Lezec, *Nat. Commun.* **2014**, *5*, 4141.
[22] J. S. T. Smalley, F. Vallini, B. Kante, Y. Fainman, *Opt. Express* **2014**, *22*, 21088.
[23] J. Yao, Z. Liu, Y. Liu, Y. Wang, C. Sun, G. Bartal, A. M. Stacy, X. Zhang, *Science* **2008**, *321*, 930.
[24] A. V. Kabashin, P. Evans, S. Pastkovsky, W. Hendren, G. A. Wurtz, R. Atkinson, R. Pollard, V. A. Podolskiy, A. V. Zayats, *Nat. Mater.* **2009**, *8*, 867.
[25] E. J. Smith, Z. Liu, Y. Mei, O. G. Schmidt, *Nano Lett.* **2010**, *10*, 1.
[26] R. Menon, V. Gupta, H. H. Tan, K. Sreenivas, C. Jagadish, *J. Appl. Phys.* **2011**, *109*, 064905.
[27] A. K. Srivastava, J. Kumar, *Sci. Technol. Adv. Mater.* **2013**, *14*, 065002.
[28] U. Ilyas, R. S. Rawat, T. L. Tan, P. Lee, R. Chen, H. D. Sun, F. Li, S. Zhang, *J. Appl. Phys.* **2011**, *110*, 093522.
[29] T. Nagase, T. Ooie, H. Kominami, Y. Nakanishi, N. Mizutani, *Jpn. J. Appl. Phys.* **2003**, *42*, 1179.
[30] G. Luka, T. A. Krajewski, B. S. Witkowski, G. Wisz, I. S. Virt, E. Guziewicz, M. Godlewski, *J. Mater. Sci.: Mater. Electron.* **2011**, *22*, 1810.
[31] D. J. Lee, H. M. Kim, J. Y. Kwon, H. Choi, S.H. Kim, K.B. Kim, *Adv. Funct. Mater.* **2011**, *21*, 448.
[32] J. H. Hu, R. G. Gordon, *J. Appl. Phys.* **1992**, *71*, 880.
[33] H. Agura, A. Suzuki, T. Matsushita, T. Aoki, M. Okuda, *Thin Solid Films* **2003**, *445*, 263.
[34] J. G. Lu, S. Fujita, T. Kawaharamura, H. Nishinaka, Y. Kamada, T. Ohshima, Z. Z. Ye, Y. J. Zeng, Y. Z. Zhang, L. P. Zhu, H. P. He, B. H. Zhao, *J. Appl. Phys.* **2007**, *101*, 083705.
[35] V. J. Norman, *Aust. J. Chem.* **1969**, *22*, 325.
[36] J. H. Shi, S. M. Huang, J. B. Chu, H. B. Zhu, Z. A. Wang, X. D. Li, D. W. Zhang, Z. Sun, W. J. Cheng, F. Q. Huang, X. J. Yin, *J. Mater. Sci.: Mater. Electron.* **2010**, *21*, 1005.
[37] J. L. Wu, Y. C. Chen, H. Y. Lin, S. Y. Chu, C. C. Chang, C. J. Wu, Y. D. Juang, *IEEE Trans. Electron Devices* **2013**, *60*, 2324.
[38] A. J. Hoffman, L. Alekseyev, S. S. Howard, K. J. Franz, D. Wasserman, V. A. Podolskiy, E. E. Narimanov, D. L. Sivco, C. Gmachl, *Nat. Mater.* **2007**, *6*, 946.
[39] C. Argyropoulos, N. M. Estakhri, F. Monticone, A. Alu, *Opt. Express* **2013**, *21*, 15037.
[40] A. Yariv, P. Yeh, *Photonics: Optical Electronics in Modern Communication*, Oxford University, New York **2007**.
[41] M. G. Silveirinha, *Phys. Rev. B* **2009**, *79*, 153109.
[42] D. Y. K. Ko, J. C. Inkson, *Phys. Rev. B* **1988**, *38*, 9945.
[43] F. Krayzel, R. Polles, A. Moreau, M. Mihailovic, G. Granet, *J. Eur. Opt. Soc., Rapid Publ.* **2010**, *5*, 10025.
[44] C. M. Hsu, S. T. Connor, M. X. Tang, Y. Cui, *Appl. Phys. Lett.* **2008**, *93*, 133109.
[45] W. Stöber, A. Fink, E. Bohn, *J. Colloid Interface Sci.* **1968**, *26*, 62.

Received: June 22, 2015
Revised: October 7, 2015
Published online: December 30, 2015

